

1 This manuscript is a preprint and has been submitted to *AAPG Bulletin*. This manuscript has
2 not undergone peer review. Subsequent versions of this manuscript may have different
3 content. If accepted, the final accepted version of this manuscript will be available via the
4 'Peer-reviewed Publication' DOI link on the right-hand side of this webpage. Please feel free
5 to contact any of the authors directly to comment on the manuscript. We welcome any
6 feedback!

7 Subsurface temperature from seismic reflection
8 data: application to the post break up sequence
9 offshore Namibia

10 **Arka Dyuti Sarkar**¹ (arkadyuti.sarkar@manchester.ac.uk) – *Corresponding author*

11 **Mads Huuse**¹ (mads.huuse@manchester.ac.uk)

12 ¹Department of Earth and Environmental Sciences, The University of Manchester,
13 Williamson Building, Oxford Road, Manchester, M13 9PL.

14 **Acknowledgements**

15 The authors would like to thank Serica Energy and Spectrum ASA (now TGS) for provision of
16 seismic data utilised as part of this research. We would like to thank Schlumberger for the
17 provision of the Petrel licenses. We would also like to thank Kofi Owusu, Andrew Newton,
18 David Hodgetts, and Benedict Campbell for their assistance with key sections of the project.
19 Thanks also go to ADS's parents for their generous funding of his research.

20 **Abstract**

21 Accurate estimations of present-day subsurface temperatures are of critical importance to
22 the energy industry, in particular with regards to geothermal energy and petroleum
23 exploration. This paper uses seismic reflection observations of bottom-simulating reflections
24 and subsurface velocities coupled with an empirical velocity to thermal conductivity
25 transform to estimate subsurface temperature in a process dubbed reflection seismic

26 thermometry. The case study is a frontier passive margin extending from the shelf edge to
27 deep water in the central Lüderitz Basin, offshore Namibia. The bottom simulating reflector
28 is used to derive surface heat flow. The thermal conductivity model was applied to seismic
29 processing velocities to determine the subsurface thermal conductivity. Knowledge of surface
30 heat flow and thermal conductivity structure allowed us to estimate subsurface temperatures
31 across the study area. The results suggest the Lüderitz Basin has a working hydrocarbon
32 system with the inferred Aptian Kudu source interval within the gas generation window.

33 Introduction

34 Subsurface temperature is a key parameter in subsurface energy extraction from petroleum-
35 and geothermal systems (Harper, 1971; Thompson, 1979; Hunt, 1984; Bonté et al., 2012).
36 Accurate estimations of present-day subsurface temperatures are thus of critical importance
37 to the energy industry. In frontier areas, petroleum source rock maturity is a key uncertainty
38 and without access to bottom hole temperature (BHT) readings from boreholes, source rock
39 characterisation is reliant on estimation and extrapolation. A crucial component of
40 understanding the subsurface temperature field is how heat is transferred (i.e. heat flow and
41 thermal conductivity) (Sclater et al., 1980). Often there is limited understanding of the
42 variation in thermal conductivity both vertically and laterally in the subsurface domain due to
43 the difficulty collecting such data. Prior to entry into frontier basins, it is advantageous to
44 determine the source rock deliverability in the area. This is primarily controlled by two factors
45 namely source rock type and temperature history. Along many passive margins the source
46 rocks are at maximum burial depth and thus maximum temperature at the present day.
47 Present day subsurface temperatures are typically acquired from temperature probe

48 measurements that have been acquired through borehole drilling (Fuchs and Balling, 2016).
49 To estimate heat flow and temperature information in adjacent areas often involves the
50 deployment of multiple seafloor probes prior to the drilling stage (Davis et al., 2003). This
51 then requires the extrapolation of data from nearby boreholes using structural and
52 stratigraphic models (Davies and Davies, 2010). This methodology underutilises the available
53 seismic datasets that are often acquired during the early stages of exploration in frontier
54 basins. This paper presents a reflection seismic thermometry workflow for using seismic
55 reflection data to estimate subsurface temperature before drilling and applies this to a
56 frontier exploration setting.

57 It has been shown that gas hydrate identification on seismic reflection data through detection
58 of bottom simulating reflectors (BSRs) at the base of gas hydrate stability zone (GHSZ), can be
59 used for geothermal gradient estimation (Yamano et al., 1982; Calvès et al., 2010; Hodgson
60 et al., 2014; Serié et al., 2017).

61 The reflection seismic thermometry workflow predicts subsurface temperatures by first
62 estimating surface heat flow from BSRs and then utilizing seismic processing velocities to
63 derive thermal conductivity through an empirical transform. This empirical relationship
64 relating acoustic velocity and thermal conductivity is a key component in allowing the
65 estimation of subsurface temperatures throughout the seismic volume.

66 **Figure 1**

67 *Geological setting*

68 The study area (Fig. 1) is in the Lüderitz Basin offshore Namibia, bounded by the Orange Basin
69 to the south, and the Walvis Basin to the north. It is part of the southern West African

70 continental margin. Successive rifting events from the Carboniferous onwards preceded the
71 Mesozoic opening of the South Atlantic, and the breakup of Gondwana (Bagguley and Prosser,
72 1999; Karner and Driscoll, 1999; Schmidt, 2004). The margin offshore Namibia is characterised
73 as having characteristics of both a volcanic passive margin and a non-volcanic margin end
74 members (Light et al., 1993; Gladczenko et al., 1998; Bauer et al., 2000). Asymmetric rifting
75 has resulted in significant variability in the sedimentary and subsidence history between the
76 conjugate margins with this reflected in the nature of hydrocarbons discovered in these areas
77 (Mello et al., 2011). The formation of the Walvis Ridge is contemporaneous with the extrusion
78 of the Etendeka continental flood basalts and acted as a long-lived barrier to marine flow,
79 creating restricted marine conditions to the north. These conditions promoted the formation
80 of salt basins north of the Ridge in the Albian-Aptian, and these are observed on both the
81 West African and Brazilian margins (Berger et al., 1998; Davison et al., 2012). In the Lüderitz
82 Basin multiple features such as seaward dipping reflectors (SDRs) and mass transport deposits
83 (MTDs) can be observed (Torsvik et al., 2009). There are however no seamounts within 50 km
84 (~31.1 mi) from the study area, the outer limit for hydrothermal systems to extend from such
85 a system (Sclater et al., 1980; Hasterok et al., 2011).

86 The neighbouring Orange and Walvis Basins both possess working petroleum systems with
87 gas condensate discovered in the Kudu wells and oil in the Wingat well respectively (Fig. 1)
88 (Intawong et al., 2015). The key source interval relevant for the Lüderitz Basin is the Aptian
89 age Kudu shale (Fig. 2d). The source maturity of this interval in the Lüderitz Basin is as yet
90 uncertain.

91 **Figure 2**

Gas Hydrates & Bottom Simulating Reflectors

92
93 A BSR is traditionally considered as a continuous and coherent seismic event that cross-cuts
94 the primary sedimentary features, whilst mimicking the morphology of the seabed (Calvès et
95 al., 2008; Le et al., 2015; Ruppel and Kessler, 2017; Schicks, 2018). A BSR with reverse polarity
96 and near-parallelism relative to the seabed originates from the negative acoustic impedance
97 (AI) contrast between partially frozen, gas-hydrate bearing sediment at the base of the GHSZ
98 and the underlying zone of dissociated free gas and water bearing sediment (Kvenvolden &
99 Lorenson, 2001; Paganoni et al., 2016). This variant of a BSR has been commonly noted in
100 studies globally and is usually considered a sign of hydrate presence (Shipley and Houston,
101 1979; Stoll and Bryan, 1979; Haacke et al., 2007).

Heat Flow

102
103 Understanding heat flow is crucial to building reliable geological models of both the shallow
104 and deep subsurface and has important implications for the exploration and development of
105 natural resources such as petroleum (Tissot et al., 1987). Heat flow has traditionally been
106 associated with tectonism and the thickness of the radiogenic crust. However mantle
107 processes in continental margins also impact heat flow (Goutorbe et al., 2011). Heat from the
108 mantle or primordial heat is one contributing factor to the thermal structure in sedimentary
109 basins and is the deepest source of heat production (Hokstad et al., 2017). Mantle heat flow
110 is estimated from the base of the crust, equivalent to the Moho (thus the prevalence of the
111 1330 °C (2426 °F) isotherm as a reference point in traditional bottom-up basin modelling
112 workflows). The other contribution to heat is in the form of radiogenic heat production.

113 Radiogenic elements are found in insignificant quantities in oceanic crust and lithospheric
114 mantle, therefore the radiogenic heat input will be greatest in areas of continental crust and
115 sediments (Hasterok, 2010; Allen and Allen, 2013). Basins located in the transitional zone
116 between onshore and offshore regions tend to have considerable structural variability and
117 thus as a consequence have been the least predictable for heat flow using global averages
118 only (Jaupart et al., 2016; Hokstad et al., 2017). Though young ocean crust is particularly
119 susceptible to hydrothermal fluid circulation impacting heat flow, in the Lüderitz Basin this is
120 not an issue due to the relative age of the underlying crust and proximity to the coast parallel
121 continent ocean boundary (COB) (Lister, 1972; Gladchenko et al., 1998).

122 Global coverage of heat flow data is not extensive, with surface heat flow data globally being
123 limited relative to estimates of total heat output (Gosnold & Panda, 2002; Lucazeau, 2019;
124 Macgregor, 2020). In the study area, the solitary heat flow data point is from Ocean Drilling
125 Program (ODP) Site 1084 as shown in Fig. 1. Reported values of heat flow in published
126 literature are made either through direct measurement or through estimations based on
127 crustal thickness and age (Davies and Davies, 2010; Davies, 2013). Such heat flow estimates
128 can have a threefold basis with primary data from measured data points; in oceanic crustal
129 settings, heat flow is based on crustal thickness to mitigate for measurement perturbation
130 due to fluid flow; and finally in the absence of measurements an estimate can be made on
131 the basis of geology. The Bullard method is commonly used to calculate heat flow from
132 borehole data from the relation between temperature and the thermal resistance of the
133 sediments (Bullard, 1939; Pribnow et al., 2000). For there to be a linear relationship between
134 acoustic velocity and thermal conductivity conditions downhole must be conductive, steady
135 state and with no internal heat sources. The latter is difficult as heat is introduced into the

136 system during drilling from friction with the drill bit and the circulation of drilling fluids, thus
137 necessitating time-based corrections for the impact of drilling on local thermal regime.

138 *Conventional thermal data*

139 Over large regions like continental margins, it is difficult to ensure high spatial resolution of
140 thermal data from conventional techniques such as downhole temperature measurements
141 and gravity driven thermal probes (Phrampus et al., 2017). This is both a result of scarcity of
142 boreholes and prohibitive expense. Heat flow derived from the seismic imaging of gas
143 hydrates can be useful in areas where significant bottom water temperature (BWT)
144 fluctuation adversely affects the reliability of thermal probe data or where hard ground may
145 prevent probe insertion (Hyndman et al., 2001). ODP thermal conductivity measurements on
146 core samples from gas hydrate provinces are unreliable due to gas exsolution during recovery
147 (Phrampus et al., 2017). This phenomenon depresses onboard thermal conductivity
148 measurements. For the transient line source needle probe used in ODP studies to measure
149 thermal conductivity it is important to note the orientation of the needle insertion relative to
150 the sediment bedding direction as the thermal conductivity measurement is provided for a
151 plane perpendicular to the needle axis (Pribnow et al., 2000). For shipboard temperature
152 measurements temperature-time curves are subjectively fit to APC probe data (to restore to
153 equilibrium temperatures and negate the effect of frictional heating upon insertion of the
154 probe) (Grevemeyer and Villinger, 2001).

155 The Curie isotherm is a common subsurface thermal marker sometimes representing a
156 petrophysical boundary (Langel and Hinze, 1998). It is commonly considered to be ~580 °C (~
157 1076 °F) as this is the Curie Point temperature of magnetite, the most common magnetic

158 mineral in the continental crust, especially in deeper regions (Frost and Shive, 1986). Thus,
159 the depth corresponding to a lack of magnetism is likely at temperatures in excess of the Curie
160 point of magnetite or a result of compositional changes leading to magnetite poor rocks at
161 depth (Beardsmore and Cull, 2001). However, this method simply defines a solitary
162 subsurface isotherm over a great depth interval from the seabed, thus making any linear
163 geothermal gradient calculated greatly approximated. Furthermore, for high resolution
164 estimation of the Curie isotherm depth, regional scale gravity data would be required.
165 Global thermal data coverage may also suffer from spatial bias, as there tends to be a greater
166 interest for scientists in areas of higher heat flow resulting in a greater concentration of data,
167 with another potential driving factor being interest in areas with geothermal energy
168 application (Davies, 2013).

169 Data

170 *Seismic data*

171 This study uses a combination of 2D and 3D multichannel, post-stack, time-migrated seismic
172 reflection data from offshore Namibia, covering both the shallow- and deep-water sectors of
173 the Lüderitz basin (Fig. 1). The seismic database is correlated with a single exploration well
174 located on the continental shelf, in addition to ODP Site 1084 in the deep-water area.

175 The 2D seismic data were provided by Spectrum ASA and consists of two surveys conducted
176 in 2006 and 2012 respectively, with further reprocessing in 2012 (to improve image quality in
177 legacy data and to tie 2006 vintage seismic to newly shot 2012 seismic data), and a combined
178 total line length of 752 km (~ 467 mi). The lines have a 4 ms two-way travel time (TWT) sample
179 rate. The frequency range is 3 - 206 Hz (dominant frequency ~ 90 Hz) with a common mid-

180 point (CMP) spacing of 12.5 m (~7.77 ft) and a shot interval of 25 m (~15.5 ft). 2006 vintage
181 2D seismic data was collected with a streamer length of 8100 m (~5033 ft) while 2012 vintage
182 2D seismic data was collected with a streamer length of 10500 m (~6524 ft).

183 The 3D seismic survey covers an area of 4150 km² (~1602 mi²) and was acquired for Serica
184 and partners by Polarcus in 2012 using *M/V Polarcus Nadia*. Primary objective of the survey
185 was to establish prospectivity by mapping pinch out structures and a large channel feature in
186 the study area. Streamer length was 8100 m (~5033 ft) with 50 m (~164 ft) source separation
187 of dual source (0.0695 m³ [2.45 ft³]) air guns. It is 80-fold with a 4 ms TWT sample rate and
188 Inline spacing of 12.5 m (~7.77 ft) and Xline spacing of 25 m (~15.5 ft). 3D pre-stack time
189 migration was conducted by ION GXT. The isotropic frequency range for Kirchhoff pre-stack
190 time migration (PreSTM) ranged between 3-110 Hz. All data were processed through stack
191 and time migration. Velocity model building was done using two iterations of dense residual
192 move out (RMO) auto-picking to create a smooth velocity model constrained by the geological
193 horizons. Velocity model parameters of 4 ms sample interval, 9000 ms trace length and a 6000
194 m (~19685 ft) aperture. By parameterising the final velocity model (Fig. 3) for steep dips and
195 high frequency gathers, the amplitude preserving preSTM resulted in high resolution image
196 gathers.

197 **Figure 3**

198

Well data

199 Well data included ODP Site 1084 and Norsk Hydro Exploration well 2513/8-1 (Fig. 1). The
200 ODP borehole was drilled as part of ODP Leg 175 with the primary intention of documenting
201 the migration of the Benguela Current along the South Atlantic West African Margin (Wefer
202 et al., 1998). It is located in a water depth of 1992 m (~6535 ft) and targeted the downslope
203 rim of the Lüderitz depositional basin. Useful subsurface borehole data included headspace
204 gas analysis, gas chromatography results and core data.

205 The exploration well 2513/8-1 is situated on the shelf in a water depth of 243 m (~797 ft) and
206 targeted a Lower Cretaceous lobe in a thrust ramp graben before terminating in Barremian-
207 Aptian age volcanic rocks at a total depth of 2553 m (~8376 ft). Some sparse BHT data points
208 from this well provide the only available calibration for the temperature estimation workflow.

209 **Method**

210 **Figure 4**

211 The temperature estimation workflow utilised in this study is outlined in Fig. 4 and described
212 below. The entirety of the workflow has been developed and tested using commercial
213 software developed for use in the petroleum industry (Schlumberger Petrel).

214 The gas hydrate stability field can be utilised to estimate the temperature at the base of the
215 zone of stable gas hydrates, demarcated on seismic by a BSR (Dickens and Quinby-Hunt, 1994;
216 Sloan et al., 1998; Lu and Sultan, 2008). This in turn allows a shallow geothermal gradient
217 across the GHSZ to be estimated and surface heat flow to be estimated (Minshull, 2011;
218 Priyanto, 2018). The stability conditions are controlled in part by the geochemical properties

219 of the fluids available to form clathrate hydrates, which in frontier settings with limited
 220 ground truthing are generally assumed to be average salinity (33.5 ‰) seawater and pure
 221 methane (Sloan et al., 1998). Pore fluid pressure conditions are generally assumed to be
 222 hydrostatic, equivalent to $0.0101 \text{ MPa m}^{-1}$ ($\sim 0.446 \text{ psi ft}^{-1}$). The following relationship (Eq. 1)
 223 as defined by (Dickens and Quinby-Hunt, 1994) describes methane hydrate stability:

224 **Equation 1:**
$$\frac{1}{T_{BSR}} = 3.79 \times 10^{-3} - 2.83 \times 10^{-4}(\log P)$$

225 where T_{BSR} is temperature at the base of GHSZ (K); and P is the corresponding pressure (MPa).
 226 Assuming hydrostatic pressure at the BSR depth, temperature at the base of the hydrate
 227 stability zone has been established:

228 **Equation 2:**
$$T_{BSR} = ((3.79 \times 10^{-3} - 2.83 \times 10^{-4}(\log(\rho \times g \times Z_{BSR})))^{-1}) - 273$$

229 Where T_{BSR} is the temperature at GHSZ (°C); ρ is density (kg m^{-3}) (of seawater); g is
 230 acceleration due to gravity (m s^{-2}) and Z_{BSR} is the depth (m) of the BSR. It must be noted that
 231 this is a minimum temperature estimate based on assumed stability field conditions (Dickens,
 232 2001).

233 The National Oceanic and Atmospheric Administration (NOAA) World Ocean Atlas (WOA)
 234 (Boyer et al., 2005) is an open source dataset containing data covering the world's oceans for
 235 temperature, salinity, density, etc. Seabed temperature (Eq. 3) was modelled in the study
 236 area using a synthetic hydrothermal gradient derived from the closest WOA data nodes, with
 237 the misfit from this approach amounting to $\pm 0.4 \text{ °C}$ ($\pm 0.18 \text{ °F}$) across the water column.

238 **Equation 3:**
$$T_{SEABED} = (-1.919 \ln Z + 21.899) \quad \text{if } Z \leq 200$$

 239
$$T_{SEABED} = 525.65Z^{-0.714} \quad \text{if } 200 < Z < 1000$$

 240
$$T_{SEABED} = -0.0007Z + 4.4905 \quad \text{if } Z \geq 1000$$

241 where T_{SEABED} is the modelled hydrothermal gradient temperature ($^{\circ}\text{C}$) and Z is seabed depth
242 (m).

243 Given both T_{SEABED} , Z_{SEABED} and T_{BSR} , Z_{BSR} at any geographical locality, then the geothermal
244 gradient (dT/dZ) across the GHSZ at that locality is given by the following relationship.

245 **Equation 4:**
$$\frac{dT}{dZ} GHSZ = \frac{T_{BSR} - T_{SEABED}}{Z_{BSR} - Z_{SEABED}}$$

246 Where dT/dZ is geothermal gradient ($^{\circ}\text{C km}^{-1}$); T_{BSR} is temperature at BSR ($^{\circ}\text{C}$); T_{SEABED} is seabed
247 temperature ($^{\circ}\text{C}$); Z_{BSR} is depth of BSR (km); Z_{SEABED} is seafloor depth (km).

248 Alongside thermal gradient, two key thermal properties are the heat flow and thermal
249 conductivity.

250 **Equation 5:**
$$Q = k \times \frac{dT}{dZ}$$

251 Where Q is heat flow (mWm^{-2}); k is thermal conductivity ($\text{W m}^{-1} \text{K}^{-1}$) (see Section 3.1) and
252 dT/dZ is geothermal gradient ($^{\circ}\text{C km}^{-1}$).

253 Fourier's Law of heat conduction (Eq. 5) is crucial to understanding the interplay between
254 heat flow, thermal conductivity, and geothermal gradient. Establishing a shallow linear
255 geothermal gradient using BSRs is well established (Calvès et al., 2010; Serié et al., 2017) and
256 studies have extrapolated this shallow geotherm for traditional basin modelling workflows.
257 This however does not consider the thermal conductivity structure of the subsurface and how
258 it might be possible to utilise seismic reflection velocity data to do so.

259 *Thermal conductivity estimation*

260 Thermal conductivity is a measure of how well heat is conducted through a material (Gu et
261 al., 2017). Difficulty associated with measuring thermal conductivity in boreholes arise from

262 poor contact between the measuring tool and the borehole wall (Horai, 1982). Thus,
263 considerable attention has been devoted to determining methods for estimating thermal
264 conductivity through more easily acquired secondary data such as seismic velocity
265 measurements. Experimental studies have shown that primary controls on thermal
266 conductivity include mineral composition, porosity and fractures (Gegenhuber and Schoen,
267 2012). Seismic wave velocity is also largely controlled by the same factors. Early work by
268 (Horai, 1982) sought to correlate thermal conductivity with other physical properties such as
269 water content, bulk density, porosity and compressional sound wave velocity. The direct
270 approach involves deriving thermal conductivity from physical properties via empirical
271 relationships (Zamora et al., 1993). Estimates of thermal conductivity computed directly from
272 conventional wireline data can be accurate within $0.2 - 0.3 \text{ W m}^{-1} \text{ K}^{-1}$ ($\sim 0.116 - 0.173 \text{ BTU h}^{-1}$
273 $\text{ft}^{-1} \text{ }^\circ\text{F}^{-1}$) when derived using empirical relationships from sonic velocity data (Hartmann et al.,
274 2005). Such a direct approach has been utilised in this work using experimental data from
275 existing correlation studies (Brigaud et al., 1990; Brigaud & Vasseur, 1989; Esteban et al.,
276 2015; Griffiths et al., 1992; Gunn et al., 2005; Kukkonen & Peltoniemi, 1998; Francis Lucazeau
277 et al., 2004; Mielke et al., 2017; Popov et al., 2003; Popov et al., 1999). Such a direct empirical
278 approach derived from experimental data has also been tested by the authors in other basins
279 (Sarkar, 2020; Sarkar and Huuse, 2021).

280 Experimental data can vary in terms of the conditions under which it was collected. Most
281 measurements have been taken at ambient pressure and temperature conditions. Binary
282 parameterisation of the experimental datasets allows characterisation of data points
283 collected under similar parameters. Most studies measured thermal conductivity using the

284 optical scanning method (Popov et al., 1999). There are fewer instances in the source datasets
285 of the use of the divided bar method of measuring thermal conductivity (Hyndman and
286 Jolivet, 1976; Evans, 1977). Only wet samples from these studies were used as our case study
287 is in deep water and thus fully saturated with water, gas and/or gas hydrate. In dry samples,
288 the contribution to thermal conductivity arising from lithological heterogeneities (matrix
289 properties) can be masked by the stronger influence of porosity (Hartmann et al., 2005). In
290 contrast wet samples reflect the impact of porosity and lithological variations.

291 The range of samples included in our fits cover a wide range of lithologies, including
292 sandstones, limestones, granites, basalts, marble to name a few (Grevemeyer and Villinger,
293 2001; Hartmann et al., 2005; Boulanouar et al., 2013; Esteban et al., 2015; Jorand et al., 2015;
294 Gu et al., 2017; Mielke et al., 2017). In so doing it is hoped that the resulting empirical
295 relationship will best apply to the broadest possible range of rock types that can be expected
296 subsurface across the study area. It must be noted though that variables within the sample
297 set (Fig. 5) include and are not limited to the porosity (arising from cracks for example).
298 Fractures are known to reduce both P wave velocities and thermal conductivity (Zamora et
299 al., 1993).

300 A regression through the filtered experimental data points taken from the aforementioned
301 studies gives the following empirical relationship for thermal conductivity:

302 **Equation 6:** $k_V = (0.001 \times V_P) - 0.5071$

303 Where k_V is thermal conductivity from velocity ($\text{W m}^{-1} \text{K}^{-1}$) and V_P is P wave velocity (m s^{-1}).

304 **Figure 5**

305 Certain trends are evident in the cross plot of sample data in Fig. 5. Due to the lack of salt
306 encountered in the study area, there is a lack of sample points in the expected high
307 conductivities associated with salt (Esteban et al., 2015). The regression is anchored by the
308 large cluster of points associated with the Grevenmeyer & Villinger (2001) data. The Hartmann
309 et al. (2005) and Gu et al. (2017) samples are parallel to the best fit regression.

310 Seismic P wave velocity within the area is converted to thermal conductivity (k_v) using the
311 thermal conductivity relationship (Eq. 6), with velocity averaged down to the depth of the
312 BSR, Z_{BSR} . The variation in thermal conductivity with depth can be overlain on a 3D seismic
313 reflection dataset in this manner. Using Z_{BSR} , determined on reflection seismic data, the
314 hydrate stability field can be utilised to compute the temperature at this phase boundary for
315 the base of the GHSZ (using Eq. 2). Temperature at the seabed is known from the
316 hydrothermal gradient (given by Eq. 3). A shallow geothermal gradient may thus be computed
317 between seabed and BSR (Eq. 4). As thermal conductivity has been derived from acoustic
318 velocity data, and with shallow geothermal gradient also available, it becomes possible to
319 reapply Fourier's Law (Eq. 5) to derive heat flow for this area through inverse modelling.
320 Estimating the shallow geotherm and heat flow along the full extent of a BSR helps eliminate
321 the bias in heat flow distribution from direct measurements taken at discrete locations
322 (Shankar and Riedel, 2013). This BSR derived heat flow proxy is used in conjunction with the
323 bulk thermal conductivity volume to generate a volume of average geothermal gradient for
324 the bulk volume (rearranging Eq. 5).

325 Temperature below the seafloor can be summarised as being a function of the depth below
326 the seafloor and the average geothermal gradient. It follows that an estimate of temperature

327 may be arrived at through this simple relationship where the temperature at any given depth
328 point is given by multiplying the average geothermal gradient against the depth to that point:

329 **Equation 7:** $T = T_{SEABED} + \left(\frac{dT}{dZ} \times Z_{SUBSURFACE}\right)$

330 where T is predicted temperature (°C); T_{SEABED} is the temperature at seabed (°C); dT/dZ is the
331 average geothermal gradient (°C km⁻¹); and $Z_{SUBSURFACE}$ is the subsurface depth (km). Seabed
332 temperature is added to account for the effect of the hydrothermal gradient on the
333 subsurface temperatures.

334 As the average geothermal gradient is only valid for the subsurface and due to the seismic
335 input volume containing the water column it becomes necessary to negate the latter. Without
336 flattening the volume to the seabed, it is instead possible to use the seabed depth map to
337 derive a depth volume relative to seabed depth.

338 **Equation 8:** $Z_{SUBSURFACE} = Z - Z_{SEABED}$

339 where $Z_{SUBSURFACE}$ is the subsurface depth (km); Z is the absolute depth (km); and Z_{SEABED} is the
340 seabed depth (km).

341 The steps outlined above are all possible using basic functions available within the Petrel
342 seismic interpretation suite. A pillar grid corresponding to the extent of the seismic survey is
343 built with voxel sizes of 50 m * 50 m * 10 m (~164 ft * 164 ft * 32.8 ft). The original seismic
344 reflection and velocity data can be resampled into the pillar grid. It must be noted that
345 resampling the original data can result in a loss of fidelity from the algorithm used and the
346 size of the voxels comprising the model. The advantage of using such a pillar grid is that
347 computation of the various properties such as velocity derived thermal conductivity (k_v)
348 become easier. It is also easier to model pseudo boreholes in this manner.

349

Uncertainty modelling

350 An attempt to model uncertainty was made following the use of 95% confidence interval
351 method as used by Phrampus et al. (2017) to derive bounds for both the heat flow proxy from
352 BSR and the overall temperature prediction. The approach to calculating these bounds can be
353 considered modular for the two aforementioned predicted thermal properties, with the same
354 workflow (Fig. 4) also used here but with an upper bound and lower bound approach for each
355 step as shown in Table 1. For example, to model the lower bound of the shallow heat flow
356 proxy, firstly the lower bound of the root mean square (RMS) of interval velocity across the
357 GHSZ is used to domain convert the TWT BSR pick. This has the effect of varying the BSR in
358 depth, to a shallower depth because of the lower interval velocity selected which in turn
359 would result in a lower temperature for the BSR using the phase relationship described
360 previously. It must be noted that the hydrate phase composition is not varied and that the
361 pressure field is unaltered from previous modelling. Similarly, the seabed depth and
362 temperature are considered unchanged. This gives the lower bound for geothermal gradient.
363 Using the 1D approximation of Fourier's law (Eq. 5) this lower bound geothermal gradient is
364 convolved with the lower bound regression for thermal conductivity from velocity separate
365 from that discussed in Section 3.1 but based on the same 95% confidence interval. This results
366 in the lower bound of the heat flow estimate from the BSR. Using the opposite bound of the
367 various component steps helps arrive at the upper bound for heat flow. The bounds for the
368 temperature prediction can be simplified to varying the bulk thermal conductivity volume and
369 conditioning the model with the upper and lower bound heat flow from BSR. This gives an

370 envelope of temperatures representing the spread of values possible using 95% confidence
371 for all input parameters.
372

373 **Table 1**

374 **Results**

375 The BSR observed in the area has been mapped across the NW and SW quadrants of the 3D
376 reflection seismic coverage (Fig. 6). Though the full extent of the visible BSR was mapped, only
377 the extent corresponding to the highest confidence seismic picks are displayed as the clarity
378 of the BSR degrades towards the edges. This should preclude any resulting anomalous
379 artefacts and edge effects. It is this high confidence extent of the BSR that is referred to in the
380 following sections unless otherwise specified. The BSRs are found to have opposite seismic
381 reflection polarity to the seabed reflection indicating the likelihood of gas hydrate above free
382 gas (Kretschmer et al., 2015). Though there is no record of hydrates from ODP Site 1084, high
383 amplitude reflections are observed to occur in close proximity below the BSR (Fig. 2a),
384 characteristic of the presence of trapped gas. Temperature at BSR depth and the phase
385 relationship used to determine this is shown in Fig. 6.

386 **Figure 6**

387 Neither the exploration well nor ODP Site 1084 fall within the bounds of the thermal model.
388 As a result, direct calibration is not possible. However well 2513/8-1 contains BHT information
389 that may provide some calibration for the predicted results. Pseudo-wells provide a means of
390 simulating 2513/8-1 at a comparable location along strike (Fig. 1a). P1 is projected into the
391 study area following bathymetric contours as close as possible along strike from 2513/8-1, to
392 maintain structural parity. BHT recordings typically are lower than actual formation
393 temperature due to cooling effect of circulating fluids in a borehole and thus they must be
394 corrected (Deming, 1989). There are insufficient points for a Horner correction (Horner, 1951;

395 Bonté et al., 2012) to be applied and hence a rudimentary correction is made for time since
396 circulation (see <https://www.zetaware.com/utilities/bht/timesince.html> first accessed
397 August 2018). The predicted temperatures are between 17 and 26% higher than the corrected
398 BHT (Fig. 7a).

399 **Figure 7**

400 On seismic data it was evident that there is a deeply incised canyon like structure trending NE
401 – SW that can be seen in the north-eastern most extent of the seismic volume (Wanke and
402 Toirac-proenza, 2018). This corresponds to the location of P1, which is seen to intersect the
403 channel fill structures of this canyon. It becomes evident then that though P1 was projected
404 into the seismic volume maintaining bathymetric parity, in the subsurface, due to the
405 occurrence of this channel like geometry, it is not possible to maintain stratigraphic parity to
406 2513/8-1. This is surmised to be the primary factor for the misfit with BHT seen.

407 Further pseudo-wells (T1 – 3) were modelled to examine the change in thermal profile moving
408 from the proximal section to the distal part of the study area. The results (Fig. 7) display what
409 the thermal profile in these boreholes would be like should a typical geothermal gradient of
410 $30\text{ }^{\circ}\text{C km}^{-1}$ or $40\text{ }^{\circ}\text{C km}^{-1}$ was applied linearly from seabed. The temperature window
411 considered prospective for reservoirs in present day has been referred to as the Golden Zone
412 ($60 - 120\text{ }^{\circ}\text{C}$ [$140 - 248\text{ }^{\circ}\text{F}$]) (Nadeau, 2011). It becomes apparent then that the varying
413 geothermal gradient with depth of the proposed model would significantly alter the
414 subsurface depth at which the Golden Zone would begin and end in comparison to the typical
415 linear geothermal gradients that are often considered in a traditional basin modelling
416 workflow. Analysing the geothermal gradient between these pseudo-wells it is seen that in

417 the proximal section (T1) there is a much steeper drop off ($\sim 57.1 \text{ }^\circ\text{C km}^{-1}$ in the uppermost
418 800 m [$\sim 2625 \text{ ft}$] to $15 \text{ }^\circ\text{C km}^{-1}$ in the deepest 1000 m [$\sim 3281 \text{ ft}$]) compared to the
419 intermediate (T2) and deeper sections (T3). The spread of isotherms in a dip section (Fig. 8)
420 reflects this. Isotherm spacing is regular in the Mesozoic section moving into deeper water.
421 However, in the proximal end corresponding to minimal Tertiary cover, there is observed the
422 greatest divergence between isotherms in Mesozoic sediment. Temperature for the Aptian
423 'Kudu shale' source rock in the region has also been mapped (Fig. 8).

424 **Figure 8**

425 Below both BSRs, but particularly the northern BSR (Fig. 6), the effects of gas blanking were
426 observed in the seismic reflection data. An average interval velocity extraction reveals
427 anomalously low values within this area (Fig. 8). Pseudo-well T4 was modelled to capture this
428 area. The results of this borehole are consistent with the deep-water pseudo-well T3 with
429 similar geothermal gradient at each 1000 m (~3281 ft) interval between the two boreholes.

430 Discussion

431 *Uncertainty*

432 In a quantitative workflow such as the one discussed in the paper, there are multiple avenues
433 for uncertainty in the constituent steps. Previous literature includes attempts to quantify the
434 uncertainty in predictions using a BSR derived geothermal gradient (5 – 35%) and heat flow
435 (10 – 50%) (Grevemeyer and Villinger, 2001). Such attempts have usually quantified
436 uncertainty for the component steps rather than the compound uncertainty for the entire
437 process. For this work, with a lack of well data for ground truthing, the temperature
438 estimation bounds for 95% confidence were used to give an idea of the range within which
439 the estimates can vary. It is important to note the impact of variability in input factors for the
440 component steps. For example, results from the Blake Ridge show that actual temperatures
441 at the BSR depth could be between 0.5 – 2.9 °C (32.9 – 37.22 °F) lower than the temperature
442 predicted by the hydrate phase relationship for that particular depth and pressure (Wood and
443 Ruppel, 2000). This implies that a significant source of uncertainty in the thermal modelling
444 could result from the assumptions made about the conditions at the base of the GHSZ. As
445 stated earlier, an assumption has been made on the lattice fluid and trapped gas mix for the

446 hydrate zone in the absence of direct piston core sampling. Varying gas compositions can vary
447 the hydrate stability and thus alter the temperature at the bottom simulating reflector (Chand
448 et al., 2008). The prevalence of methane hydrates globally leads us to assume it is the most
449 likely composition of the hydrates in the study area.

450 BWT fluctuations, both the magnitude and time scale for which they occur provide another
451 element of uncertainty. It must be noted that the strong Benguela Current flows along the
452 Namibian margin in this area and it is difficult to directly factor in the impact that this may
453 have on the modelling. However, the data used to generate a model of the hydrothermal
454 gradient in the area utilised NOAA data that have been averaged annually over an eight-year
455 period. It thus hoped that any temporal perturbations of BWT are accounted for by this
456 dataset.

457 The quality of the initial velocity model is another source of uncertainty. As thermal
458 conductivity is derived from it using a direct empirical relationship, any anomalies in the
459 existing velocity model or velocity data will be translated into the derived properties. From
460 the low spread of RMS interval velocities for the GHSZ it is apparent the application of a
461 default 1500 m s^{-1} ($\sim 4921 \text{ ft s}^{-1}$) velocity above seabed during the velocity model building stage
462 results in a heavily smoothed velocity model. This is expected to be reflected in the nature of
463 the temperature profile generated using velocities as input.

464 In the absence of a reliable heat flow recording for this area, a BSR derived heat flow proxy
465 has been used. This is a shallow heat flow as it uses an average velocity derived thermal
466 conductivity and geothermal gradient valid within the GHSZ (Eq. 5). Unlike in traditional basin
467 modelling the radiogenic heat production of the rock column has not been integrated.

468 Instead, this solitary heat flow proxy has been used to condition the model for an average
469 geothermal gradient. Though hydrothermal fluid circulation in the subsurface can also greatly
470 alter heat flow, both vertically and laterally, the study area is likely to be minimally impacted
471 in this regard. As the study area is sufficiently distant from a neighbouring seamount to negate
472 the convective and advective heat flow impact of hydrothermal fluid circulation, heat
473 transport in this area is predominantly conductive. Therefore, the assumption is of limited
474 lateral heat flow variability, which is backed by the BSR-derived thermal gradients and
475 derivative heat flow estimates. In a separate case study covering the data rich North Sea, it
476 has been shown that the reflection seismic thermometric process can be conducted
477 successfully using laterally varying shallow heat flow as an input (Sarkar, 2020). An idea of the
478 uncertainty of the heat flow derived in this manner has been computed using the method
479 shown in Phrampus et al. (2017). Heat flow is found to range between $46.2 - 76.2 \text{ mWm}^{-2}$
480 ($\sim 0.01465 - 0.02416 \text{ BTU h}^{-1} \text{ ft}^{-2}$), with the weighted mean for the heat flow used for
481 computation of the temperature model equal to 63.8 mWm^{-2} ($\sim 0.02022 \text{ BTU h}^{-1} \text{ ft}^{-2}$). The
482 lower bound of the derived ranged is consistent with results from Macgregor (2020) while the
483 upper bound would be in line with the preferred prediction from the global map in Lucazeau
484 (2019). The weighted mean is interestingly consistent with the continental margin heat flow
485 mean reported by Davies (2013). The heat flow range given by the bounds is consistent with
486 observational data and estimations of heat flow from age relationships corresponding to this
487 area (Hamza and Vieira, 2012).

488

Implications

489 As stated previously, the source maturity of the Aptian Kudu shale interval in the Lüderitz
490 Basin is a key unknown in terms of the petroleum systems elements. With the thermal
491 modelling workflow indicating an average temperature of 133.5 °C (272.3 °F) across the top
492 of this Barremian structure (Fig. 8a), the base of the overlying Kudu shale source rock
493 immediately above would therefore lie in the gas generation window (Bjørlykke et al., 1989).
494 This is consistent with the nearby Kudu fields which produce gas condensate from the same
495 Aptian source interval. The results would suggest then that the Lüderitz Basin has an improved
496 prospectivity outlook with the potential for a working hydrocarbon system with gas charged
497 reservoirs.

498 It was possible in this study to estimate present day temperature at key subsurface target
499 depths in a frontier setting in the absence of any substantive well control. The workflow
500 presented would enable seismic operators to utilise the data libraries of seismic reflection
501 and velocity data available to them to generate present day estimations of subsurface
502 temperature in a non-invasive manner, prior to an expensive drilling campaign. It is hoped
503 that this would help streamline petroleum systems analysis and provide an additional dataset
504 for basin modellers to use with the aim of decreasing the uncertainty with which frontier
505 regions are explored.

506 Conclusions

507 The model proposed in this study is a simple and robust methodology for estimation of
508 present-day subsurface temperature in frontier areas lacking borehole control for
509 temperatures. It makes use of readily available seismic reflection and velocity data in a
510 workflow developed on an industry standard software suite. It highlights how existing

511 workflows for BSR derived heat flow may be combined with existing experimental thermal
512 conductivity and velocity data for various lithologies to develop an empirical transform that
513 may be applied to seismic velocity models. Given thermal conductivity and P wave velocity
514 have sensitivity to similar parameters, this methodology would allow the user to examine the
515 vertical and lateral variability in thermal properties in a frontier basin especially when high-
516 quality pre-SDM and FWI velocity models are available. The results of the case study
517 documented here suggest that the main prospect lies just below the golden zone and that
518 sources rocks are in the generative window.

519 References

- 520 Allen, P., and J. Allen, 2013, Basin analysis: principles and application to petroleum play
521 assessment.
- 522 Bagguley, J., and S. Prosser, 1999, The interpretation of passive margin depositional processes
523 using seismic stratigraphy: examples from offshore Namibia: Geological Society, London,
524 Special Publications, v. 153, no. 1, p. 321–344, doi:10.1144/GSL.SP.1999.153.01.20.
- 525 Bauer, K., S. Neben, B. Schreckenberger, R. Emmermann, K. Hinz, N. Fechner, K. Gohl, A.
526 Schulze, R. B. Trumbull, and K. Weber, 2000, Deep structure of the Namibia continental
527 margin as derived from integrated geophysical studies: Journal of Geophysical Research:
528 Solid Earth, v. 105, no. B11, p. 25829–25853, doi:10.1029/2000JB900227.
- 529 Beardsmore, G., and J. Cull, 2001, Crustal Heat Flow: A Guide to Measurement and Modelling:
530 doi:10.1017/S0016756803218021.
- 531 Becker, J. J. et al., 2009, Global Bathymetry and Elevation Data at 30 Arc Seconds Resolution:
532 SRTM30_PLUS: Marine Geodesy, v. 32, no. 4, p. 355–371,
533 doi:10.1080/01490410903297766.
- 534 Berger, W., G. Wefer, C. Richter, C. Lange, J. Girardeau, O. Hemelin, and Shipboard Scientific
535 Party, 1998, 17. The Angola-Benguela upwelling system: Paleoceanographic synthesis of
536 shipboard results from Leg 175: Proceedings of the Ocean Drilling Program, v. 175, p.
537 505–531.
- 538 Bjørlykke, K., M. Ramm, and G. C. Saigal, 1989, Sandstone diagenesis and porosity
539 modification during basin evolution: Geologische Rundschau, v. 78, no. 1, p. 243–268,
540 doi:10.1007/BF01988363.
- 541 Bonté, D., J. D. Van Wees, and J. M. Verweij, 2012, Subsurface temperature of the onshore
542 Netherlands: New temperature dataset and modelling: Geologie en
543 Mijnbouw/Netherlands Journal of Geosciences, v. 91, no. 4, p. 491–515,
544 doi:10.1017/S0016774600000354.

- 545 Boulanouar, A., A. Rahmouni, M. Boukalouch, A. Samaouali, Y. Géraud, M. Harnafi, and J.
546 Sebbani, 2013, Determination of Thermal Conductivity and Porosity of Building Stone
547 from Ultrasonic Velocity Measurements: *Geomaterials*, v. 03, no. 04, p. 138–144,
548 doi:10.4236/gm.2013.34018.
- 549 Boyer, T., S. Levitus, H. Garcia, R. A. Locarnini, C. Stephens, and J. Antonov, 2005, Objective
550 analyses of annual, seasonal, and monthly temperature and salinity for the World Ocean
551 on a 0.25° grid: *International Journal of Climatology*, v. 25, no. 7, p. 931–945,
552 doi:10.1002/joc.1173.
- 553 Bray, R., S. Lawrence, and R. Swart, 1998, Namibia License Blocks , Wells: *Oil and Gas Journal*,
554 v. 96, no. 32, p. 84–88.
- 555 Brigaud, F., D. S. Chapman, and S. Le Douaran, 1990, Estimating thermal conductivity in
556 sedimentary basins using lithologic data and geophysical well logs: *American Association
557 of Petroleum Geologists Bulletin*, v. 74, no. 9, p. 1459–1477, doi:10.1306/OC9B2501-
558 1710-11D7-8645000102C1865D.
- 559 Brigaud, F., and G. Vasseur, 1989, Mineralogy, porosity and fluid control on thermal
560 conductivity of sedimentary rocks: *Geophysical Journal International*, v. 98, no. 3, p. 525–
561 542, doi:10.1111/j.1365-246X.1989.tb02287.x.
- 562 Bullard, E. C., 1939, Heat flow in South Africa: *Proceedings of the Royal Society of London.*
563 *Series A. Mathematical and Physical Sciences*, v. 173, no. 955, p. 474–502,
564 doi:10.1098/rspa.1939.0159.
- 565 Calvès, G., M. Huuse, A. Schwab, and P. Clift, 2008, Three-dimensional seismic analysis of high-
566 amplitude anomalies in the shallow subsurface of the Northern Indus Fan: *Sedimentary
567 and/or fluid origin: Journal of Geophysical Research*, v. 113, no. B11, p. B11103,
568 doi:10.1029/2008JB005666.
- 569 Calvès, G., A. M. Schwab, M. Huuse, P. D. Clift, and A. Inam, 2010, Thermal regime of the
570 northwest Indian rifted margin - Comparison with predictions: *Marine and Petroleum
571 Geology*, v. 27, no. 5, p. 1133–1147, doi:10.1016/j.marpetgeo.2010.02.010.
- 572 Chand, S., J. Mienert, K. Andreassen, J. Knies, L. Plassen, and B. Fotland, 2008, Gas hydrate
573 stability zone modelling in areas of salt tectonics and pockmarks of the Barents Sea
574 suggests an active hydrocarbon venting system: *Marine and Petroleum Geology*, v. 25,
575 no. 7, p. 625–636, doi:10.1016/j.marpetgeo.2007.10.006.
- 576 Crameri, F., G. E. Shephard, and P. J. Heron, 2020, The misuse of colour in science
577 communication: *Nature Communications*, v. 11, no. 1, p. 5444, doi:10.1038/s41467-020-
578 19160-7.
- 579 Davies, J. H., 2013, Global map of solid Earth surface heat flow: *Geochemistry, Geophysics,
580 Geosystems*, v. 14, no. 10, p. 4608–4622, doi:10.1002/ggge.20271.
- 581 Davies, J. H., and D. R. Davies, 2010, Earth's surface heat flux: *Solid Earth*, v. 1, no. 1, p. 5–24,
582 doi:10.5194/se-1-5-2010.
- 583 Davis, E. E., K. Wang, K. Becker, R. E. Thomson, and I. Yashayaev, 2003, Deep-ocean
584 temperature variations and implications for errors in seafloor heat flow determinations:
585 *Journal of Geophysical Research: Solid Earth*, v. 108, no. B1, p. 1–6,
586 doi:10.1029/2001JB001695.
- 587 Davison, I., L. Anderson, and P. Nuttall, 2012, Salt deposition, loading and gravity drainage in

588 the Campos and Santos salt basins: Geological Society, London, Special Publications, v.
589 363, no. 1, p. 159–174, doi:10.1144/SP363.8.

590 Deming, D., 1989, Application of bottom-hole temperature corrections in geothermal studies:
591 Geothermics, v. 18, no. 5–6, p. 775–786, doi:10.1016/0375-6505(89)90106-5.

592 Dickens, G. R., 2001, Modeling the Global Carbon Cycle with a Gas Hydrate Capacitor:
593 Significance for the Latest Paleocene Thermal Maximum, *in* C. K. Paull, and W. P. Dillon,
594 eds., Natural gas hydrates: occurrence, distribution, and detection: Washington, D. C.,
595 AGU, p. 19–38, doi:10.1029/GM124p0019.

596 Dickens, G. R., and M. S. Quinby-Hunt, 1994, Methane hydrate stability in seawater:
597 Geophysical Research Letters, v. 21, no. 19, p. 2115–2118, doi:10.1029/94GL01858.

598 Esteban, L., L. Pimienta, J. Sarout, C. D. Piane, S. Haffen, Y. Geraud, and N. E. Timms, 2015,
599 Study cases of thermal conductivity prediction from P-wave velocity and porosity:
600 Geothermics, v. 53, p. 255–269, doi:10.1016/j.geothermics.2014.06.003.

601 Evans, T. R., 1977, Thermal Properties of North Sea Rocks.: Log Analyst, v. 18, no. 2, p. 3–12.

602 Frost, B. R., and P. N. Shive, 1986, Magnetic mineralogy of the lower continental crust: Journal
603 of Geophysical Research, v. 91, no. B6, p. 6513, doi:10.1029/JB091iB06p06513.

604 Fuchs, S., and N. Balling, 2016, Improving the temperature predictions of subsurface thermal
605 models by using high-quality input data. Part 2: A case study from the Danish-German
606 border region: Geothermics, v. 64, p. 1–14, doi:10.1016/j.geothermics.2016.04.004.

607 Gegenhuber, N., and J. Schoen, 2012, New approaches for the relationship between
608 compressional wave velocity and thermal conductivity: Journal of Applied Geophysics, v.
609 76, p. 50–55, doi:10.1016/j.jappgeo.2011.10.005.

610 Gladchenko, T. P., J. Skogseid, and O. Eldhom, 1998, Namibia volcanic margin: Marine
611 Geophysical Researches, v. 20, no. 4, p. 313–341, doi:10.1023/A:1004746101320.

612 Gosnold, W., and B. Panda, 2002, The Global Heat Flow Database of the International Heat
613 Flow Commission: doi:http://doi.org/10.17616/R3G305.

614 Goutorbe, B., J. Poort, F. Lucazeau, and S. Raillard, 2011, Global heat flow trends resolved
615 from multiple geological and geophysical proxies: Geophysical Journal International, v.
616 187, no. 3, p. 1405–1419, doi:10.1111/j.1365-246X.2011.05228.x.

617 Grevemeyer, I., and H. Villinger, 2001, Gas hydrate stability and the assessment of heat flow
618 through continental margins: Geophysical Journal International, v. 145, p. 647–660,
619 doi:ISI:000169428800007.

620 Griffiths, C. M., N. R. Brereton, R. Beausillon, and D. Castillo, 1992, Thermal conductivity
621 prediction from petrophysical data: a case study: Geological Applications of Wireline
622 Logs II, v. 65, no. 1, p. 299–315, doi:10.1144/GSL.SP.1992.065.01.23.

623 Gu, Y., W. Rühaak, K. Bär, and I. Sass, 2017, Using seismic data to estimate the spatial
624 distribution of rock thermal conductivity at reservoir scale: Geothermics, v. 66, p. 61–72,
625 doi:10.1016/j.geothermics.2016.11.007.

626 Gunn, D. A., L. D. Jones, M. G. Raines, D. C. Entwisle, and P. R. N. Hobbs, 2005, Laboratory
627 measurement and correction of thermal properties for application to the rock mass:
628 Geotechnical and Geological Engineering, v. 23, no. 6, p. 773–791, doi:10.1007/s10706-
629 003-3156-6.

630 Haacke, R. R., G. K. Westbrook, and R. D. Hyndman, 2007, Gas hydrate, fluid flow and free gas:
631 Formation of the bottom-simulating reflector: *Earth and Planetary Science Letters*, v.
632 261, no. 3–4, p. 407–420, doi:10.1016/j.epsl.2007.07.008.

633 Hamza, V. M., and F. P. Vieira, 2012, Global distribution of the lithosphere-asthenosphere
634 boundary: A new look: *Solid Earth*, v. 3, no. 2, p. 199–212, doi:10.5194/se-3-199-2012.

635 Harper, M. L., 1971, Approximate geothermal gradients in the North Sea basin: *Nature*, v. 230,
636 no. 5291, p. 235–236, doi:10.1038/230235a0.

637 Hartmann, A. A., V. Rath, and C. Clauser, 2005, Thermal conductivity from core and well log
638 data: *International Journal of Rock Mechanics and Mining Sciences*, v. 42, no. 7- 8 SPEC.
639 ISS., p. 1042–1055, doi:10.1016/j.ijrmms.2005.05.015.

640 Hasterok, D., 2010, Thermal State of Continental and Oceanic Lithosphere: The University of
641 Utah, 168 p.

642 Hasterok, D., D. S. Chapman, and E. E. Davis, 2011, Oceanic heat flow: Implications for global
643 heat loss: *Earth and Planetary Science Letters*, v. 311, no. 3–4, p. 386–395,
644 doi:10.1016/j.epsl.2011.09.044.

645 Hodgson, N., A. Intawong, K. Rodriguez, and M. Huuse, 2014, A seismic tool to reduce source
646 maturity risk in unexplored basins: *First Break*, v. 32, no. 3, p. 103–108.

647 Hokstad, K., Z. A. Tašárová, S. A. Clark, R. Kyrkjebø, K. Duffaut, C. Fichler, and T. Wiik, 2017,
648 Radiogenic heat production in the crust from inversion of gravity and magnetic data:
649 *Norsk Geologisk Tidsskrift*, v. 97, no. 3, p. 241–254, doi:10.17850/njg97-3-04.

650 Horai, K., 1982, Thermal Conductivity of Sediments and Igneous Rocks Recovered during Deep
651 Sea Drilling Project Leg 60, *in* D. M. Hussong, and S. Uyeda, eds., *Initial Reports of the*
652 *Deep Sea Drilling Project, 60*: U.S. Government Printing Office, p. 807–834,
653 doi:10.2973/dsdp.proc.60.149.1982.

654 Horner, D. R., 1951, Pressure build-up in wells, *in* 3rd World Petroleum Congress Proceedings:
655 p. WPC-4135.

656 Hunt, J. M., 1984, Generation and Migration of Light Hydrocarbons: *Science*, v. 226, no. 4680,
657 p. 1265–1270, doi:10.1126/science.226.4680.1265.

658 Hyndman, R. D., and J. Jolivet, 1976, Heat Flow Measurements in Deep Crustal Holes on the
659 Mid-Atlantic Ridge: v. 81, no. 23, p. 4053–4060.

660 Hyndman, R. D., G. D. Spence, R. Chapman, M. Riedel, and R. N. Edwards, 2001, Geophysical
661 Studies of Marine Gas Hydrate in Northern Cascadia, *in* C. K. Paull, and W. P. Dillon, eds.,
662 *Natural Gas Hydrates: Occurrence, Distribution, and Detection*: Washington, D. C., AGU,
663 p. 273–295, doi:10.1029/GM124p0273.

664 Intawong, A., M. Huuse, K. Rodriguez, N. Hodgson, and M. Negonga, 2015, Further de-risking
665 source rock maturity in the Luderitz Basin using basin modelling to support the BSR-
666 derived near-surface geotherm: *First Break*, v. 33, no. October, p. 71–76.

667 Jaupart, C., J. C. Mareschal, and L. Jorand, 2016, Radiogenic heat production in the
668 continental crust: *Lithos*, v. 262, p. 398–427, doi:10.1016/j.lithos.2016.07.017.

669 Jorand, R., C. Clauser, G. Marquart, and R. Pechnig, 2015, Statistically reliable petrophysical
670 properties of potential reservoir rocks for geothermal energy use and their relation to
671 lithostratigraphy and rock composition: The NE Rhenish Massif and the Lower Rhine

- 672 Embayment (Germany): *Geothermics*, v. 53, p. 413–428,
673 doi:10.1016/j.geothermics.2014.08.008.
- 674 Karner, G. D., and N. W. Driscoll, 1999, Tectonic and stratigraphic development of the West
675 African and eastern Brazilian Margins: insights from quantitative basin modelling:
676 Geological Society, London, Special Publications, v. 153, no. 1, p. 11–40,
677 doi:10.1144/GSL.SP.1999.153.01.02.
- 678 Kretschmer, K., A. Biastoch, L. Rüpke, and E. Burwicz, 2015, Modeling the fate of methane
679 hydrates under global warming: *Global Biogeochemical Cycles*, v. 29, no. 5, p. 610–625,
680 doi:10.1002/2014GB005011.
- 681 Kukkonen, I. T., and S. Peltoniemi, 1998, Relationships between thermal and other
682 petrophysical properties of rocks in Finland: *Physics and Chemistry of the Earth*, v. 23,
683 no. 3, p. 341–349, doi:10.1016/S0079-1946(98)00035-4.
- 684 Kvenvolden, K. A., and T. D. Lorenson, 2001, The Global Occurrence of Natural Gas Hydrate,
685 *in* C. K. Paull, and W. P. Dillon, eds., *Natural Gas Hydrates: Occurrence, Distribution, and*
686 *Detection*: Washington, D. C., AGU, p. 3–18, doi:10.1029/GM124p0003.
- 687 Langel, R. A., and W. J. Hinze, 1998, *The magnetic field of the Earth's lithosphere: the satellite*
688 *perspective*: Cambridge University Press, 429 p., doi:10.1029/99eo00111.
- 689 Le, A. N., M. Huuse, J. Redfern, R. L. Gawthorpe, and D. Irving, 2015, Seismic characterization
690 of a Bottom Simulating Reflection (BSR) and plumbing system of the Cameroon margin,
691 offshore West Africa: *Marine and Petroleum Geology*, v. 68, p. 629–647,
692 doi:10.1016/j.marpetgeo.2014.12.006.
- 693 Light, M. P. R., M. P. Maslanyj, R. J. Greenwood, and N. L. Banks, 1993, Seismic sequence
694 stratigraphy and tectonics offshore Namibia: *Tectonics and seismic sequence*
695 *stratigraphy*, v. 71, no. 1, p. 163–191, doi:10.1144/GSL.SP.1993.071.01.08.
- 696 Lister, C. R. B., 1972, On the Thermal Balance of a Mid-Ocean Ridge: *Geophysical Journal*
697 *International*, v. 26, no. 5, p. 515–535, doi:10.1111/j.1365-246X.1972.tb05766.x.
- 698 Locarnini, R. A. et al., 2013, *WORLD OCEAN ATLAS 2013: Temperature Volume 1*: 52 p.,
699 doi:10.7289/V55X26VD.
- 700 Lu, Z., and N. Sultan, 2008, Empirical expressions for gas hydrate stability law, its volume
701 fraction and mass-density at temperatures 273.15K to 290.15K: *Geochemical Journal*, v.
702 42, no. 2, p. 163–175, doi:10.2343/geochemj.42.163.
- 703 Lucazeau, F., 2019, Analysis and Mapping of an Updated Terrestrial Heat Flow Data Set:
704 *Geochemistry, Geophysics, Geosystems*, v. 20, no. 8, p. 4001–4024,
705 doi:10.1029/2019GC008389.
- 706 Lucazeau, F., F. Brigaud, and J. L. Bouroulllec, 2004, High-resolution heat flow density in the
707 lower Congo basin: *Geochemistry, Geophysics, Geosystems*, v. 5, no. 3, p. Q03001,
708 doi:10.1029/2003GC000644.
- 709 Macgregor, D. S., 2020, Regional variations in geothermal gradient and heat flow across the
710 African plate: *Journal of African Earth Sciences*, v. 171, p. 103950,
711 doi:10.1016/j.jafrearsci.2020.103950.
- 712 Mello, M. R., A. A. Bender, N. C. A. Filho, S. Barbanti, M. R. Franke, and C. L. C. Jesus, 2011,
713 Correlation of the Petroleum System from Santos and Namibian Offshore Basins, *in* *OTC*
714 *Brasil: Offshore Technology Conference*, p. 1–16, doi:10.4043/22813-MS.

- 715 Mielke, P., K. Bär, and I. Sass, 2017, Determining the relationship of thermal conductivity and
716 compressional wave velocity of common rock types as a basis for reservoir
717 characterization: *Journal of Applied Geophysics*, v. 140, p. 135–144,
718 doi:10.1016/j.jappgeo.2017.04.002.
- 719 Minshull, T. A., 2011, Some comments on the estimation of geothermal gradients from the
720 depths of bottom simulating reflectors, *in* Proceedings of the 7th international
721 conference on gas hydrates: p. 1–8.
- 722 Nadeau, P. H., 2011, Earth’s energy “Golden Zone”: a synthesis from mineralogical research:
723 *Clay Minerals*, v. 46, no. 1, p. 1–24, doi:10.1180/claymin.2011.046.1.1.
- 724 Paganoni, M., J. A. Cartwright, M. Foschi, R. C. Shipp, and P. Van Rensbergen, 2016, Structure
725 II gas hydrates found below the bottom-simulating reflector: *Geophysical Research*
726 *Letters*, v. 43, no. 11, p. 5696–5706, doi:10.1002/2016GL069452.
- 727 Phrampus, B. J., R. N. Harris, and A. M. Tréhu, 2017, Heat flow bounds over the Cascadia
728 margin derived from bottom simulating reflectors and implications for thermal models
729 of subduction: *Geochemistry, Geophysics, Geosystems*, v. 18, no. 9, p. 3309–3326,
730 doi:10.1002/2017GC007077.
- 731 Popov, Y. A., D. F. C. Pribnow, J. H. Sass, C. F. Williams, and H. Burkhardt, 1999,
732 Characterization of rock thermal conductivity by high-resolution optical scanning:
733 *Geothermics*, v. 28, no. 2, p. 253–276, doi:10.1016/S0375-6505(99)00007-3.
- 734 Popov, Y., V. Tertychnyi, R. Romushkevich, D. Korobkov, and J. Pohl, 2003, Interrelations
735 Between Thermal Conductivity and Other Physical Properties of Rocks: Experimental
736 Data: *Pure and Applied Geophysics*, v. 160, no. 5, p. 1137–1161,
737 doi:10.1007/PL00012565.
- 738 Pribnow, D. F. C., M. Kinoshita, and C. . Stein, 2000, Thermal data collection and heat flow
739 recalculations for ODP Legs 101-180: 1–25 p.
- 740 Priyanto, B., 2018, Heat Flow Estimation from BSR: An Example from the Aru Region, Offshore
741 West Papua, Eastern Indonesia, *in* Proc. Indonesian petrol. Assoc., 39th Ann. Conv.:
742 Indonesian Petroleum Association (IPA), p. 11, doi:10.29118/IPA.0.15.G.267.
- 743 Ruppel, C. D., and J. D. Kessler, 2017, The interaction of climate change and methane
744 hydrates: *Reviews of Geophysics*, v. 55, no. 1, p. 126–168, doi:10.1002/2016RG000534.
- 745 Sarkar, A. D., 2020, Reflection Seismic Thermometry: University of Manchester, 333 p.,
746 doi:10.31237/osf.io/fk7pb.
- 747 Sarkar, A. D., and M. Huuse, 2021, Reflection Seismic Thermometry: Basin Research, v. in
748 press.
- 749 Schicks, J. M., 2018, Gas Hydrates: Formation, Structures, and Properties, *in* H. Wilkes, ed.,
750 Hydrocarbons, Oils and Lipids: Diversity, Origin, Chemistry and Fate. Handbook of
751 Hydrocarbon and Lipid Microbiology: Springer, Cham, p. 81–95,
752 doi:doi.org/10.1007/978-3-319-54529-5_2-1.
- 753 Schmidt, S., 2004, The Petroleum Potential of the Passive Continental Margin of South-
754 Western Africa – A Basin Modelling Study: Unpublished PhD dissertation, Fakultät für
755 Georessourcen und Materialtechnik der Rheinisch-Westfälischen Technischen
756 Hochschule Aachen, Germany., 182 p.
- 757 Sclater, J. G., C. Jaupart, and D. Galson, 1980, The heat flow through oceanic and continental

758 crust and the heat loss of the Earth: *Reviews of Geophysics*, v. 18, no. 1, p. 269–311,
759 doi:10.1029/RG018i001p00269.

760 Serié, C., M. Huuse, N. H. Schødt, J. M. Brooks, and A. Williams, 2017, Subsurface fluid flow in
761 the deep-water Kwanza Basin, offshore Angola: *Basin Research*, v. 29, no. 2, p. 149–179,
762 doi:10.1111/bre.12169.

763 Shankar, U., and M. Riedel, 2013, Heat flow and gas hydrate saturation estimates from
764 Andaman Sea, India: *Marine and Petroleum Geology*, v. 43, p. 434–449,
765 doi:10.1016/j.marpetgeo.2012.12.004.

766 Shipley, T. H., and M. H. Houston, 1979, Seismic Evidence for Widespread Possible Gas
767 Hydrate Horizons on Continental Slopes and Rises: *AAPG Bulletin*, v. 63, no. 12, p. 2204–
768 2213, doi:10.1306/2F91890A-16CE-11D7-8645000102C1865D.

769 Sloan, E. D., S. Subramanian, P. N. Matthews, J. P. Lederhos, and A. A. Khokhar, 1998,
770 Quantifying Hydrate Formation and Kinetic Inhibition: *Industrial & Engineering*
771 *Chemistry Research*, v. 37, no. 8, p. 3124–3132, doi:10.1021/ie970902h.

772 Stoll, R. D., and G. M. Bryan, 1979, Physical properties of sediments containing gas hydrates:
773 *Journal of Geophysical Research*, v. 84, no. B4, p. 1629–1634,
774 doi:10.1029/JB084iB04p01629.

775 Thompson, K. F. ., 1979, Light hydrocarbons in subsurface sediments: *Geochimica et*
776 *Cosmochimica Acta*, v. 43, no. 5, p. 657–672, doi:10.1016/0016-7037(79)90251-5.

777 Tissot, B. P., R. Pelet, and P. H. Ungerer, 1987, Thermal History of Sedimentary Basins,
778 Maturation Indices, and Kinetics of Oil and Gas Generation: *AAPG Bulletin*, v. 71, no. 12,
779 p. 1445–1466, doi:10.1306/703C80E7-1707-11D7-8645000102C1865D.

780 Torsvik, T. H., S. Rouse, C. Labails, and M. A. Smethurst, 2009, A new scheme for the opening
781 of the South Atlantic Ocean and the dissection of an Aptian salt basin: *Geophysical*
782 *Journal International*, v. 177, no. 3, p. 1315–1333, doi:10.1111/j.1365-
783 246X.2009.04137.x.

784 Waite, W. F. et al., 2009, Physical properties of hydrate-bearing sediments: *Reviews of*
785 *Geophysics*, v. 47, no. 4, p. RG4003, doi:10.1029/2008RG000279.

786 Wanke, A. W., and R. Toirac-proenza, 2018, Seismic Architecture of Outer Shelf Canyon
787 Segments in the Lüderitz Basin, Offshore Namibia, *in* 2018 AAPG International
788 Conference and Exhibition: doi:10.1306/11222Wanke2019.

789 Wefer, G., W. H. Berger, and C. Richter, 1998, Site 1084, *in* G. Wefer, W. H. Berger, and C.
790 Richter, eds., *Proceedings of the Ocean Drilling Program 175 Initial Reports: Ocean*
791 *Drilling Program*, p. 339–384, doi:10.2973/odp.proc.ir.175.112.1998.

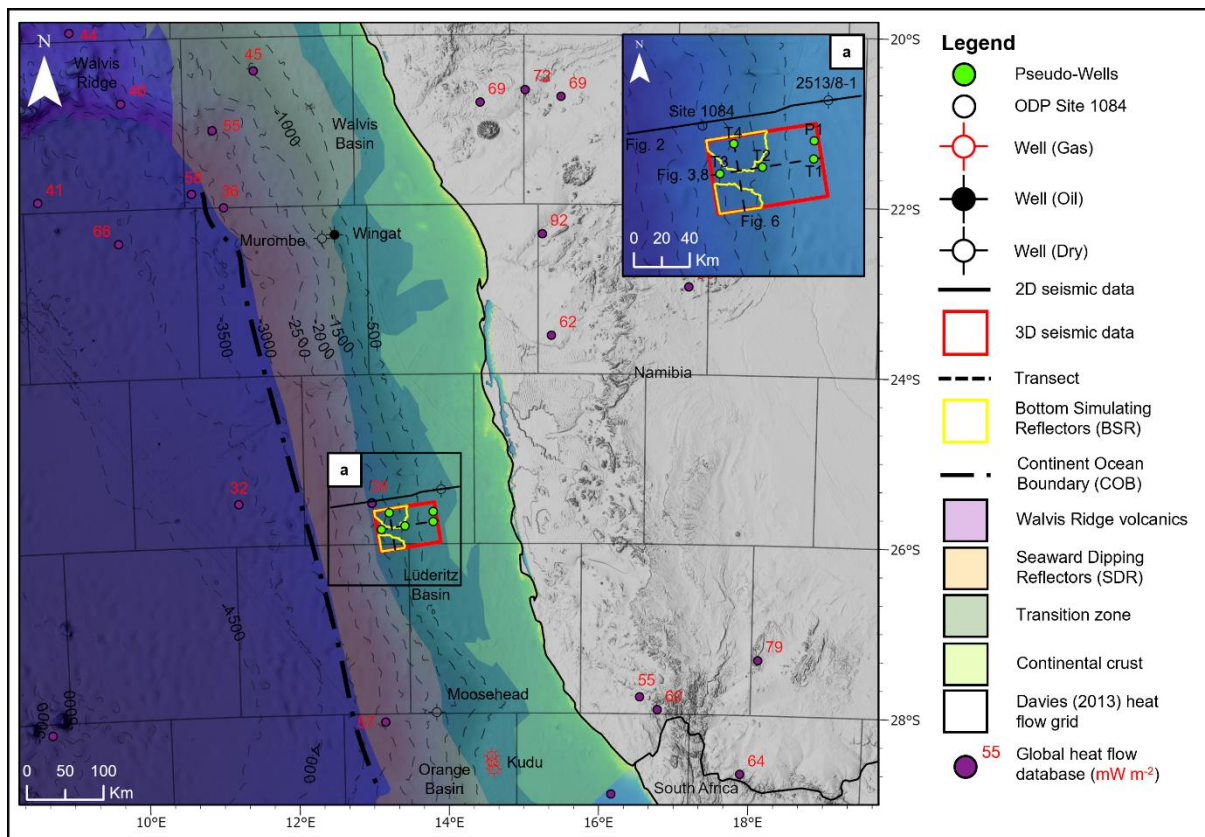
792 Wood, W. T., and C. Ruppel, 2000, Seismic and thermal investigations of the Blake Ridge gas
793 hydrate area: A synthesis, *in* C. K. Paull, R. Matusmoto, P. J. Wallace, and W. P. Dillon,
794 eds., *Proceedings of the Ocean Drilling Program: Scientific Results*: p. 253–264,
795 doi:10.2973/odp.proc.sr.164.203.2000.

796 Yamano, M., S. Uyeda, Y. Aoki, and T. H. Shipley, 1982, Estimates of heat flow derived from
797 gas hydrates: *Geology*, v. 10, no. 7, p. 339, doi:10.1130/0091-
798 7613(1982)10<339:EOHFDF>2.0.CO;2.

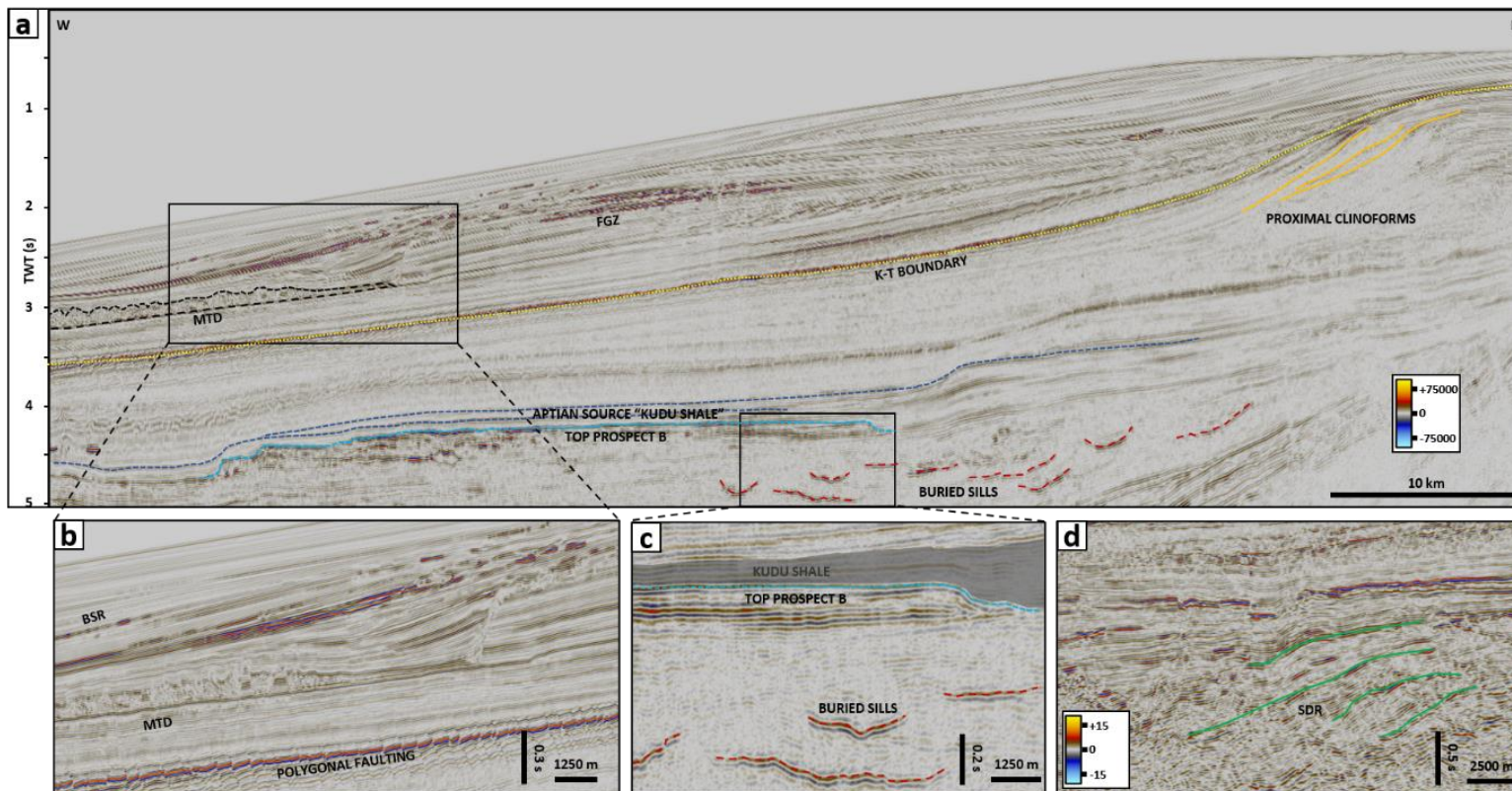
799 Zamora, M., D. Vo-Thanh, G. Bienfait, and J. P. Poirier, 1993, An empirical relationship
800 between thermal conductivity and elastic wave velocities in sandstone: *Geophysical*

801 Research Letters, v. 20, no. 16, p. 1679–1682, doi:10.1029/92GL02460.
802

803 Figures

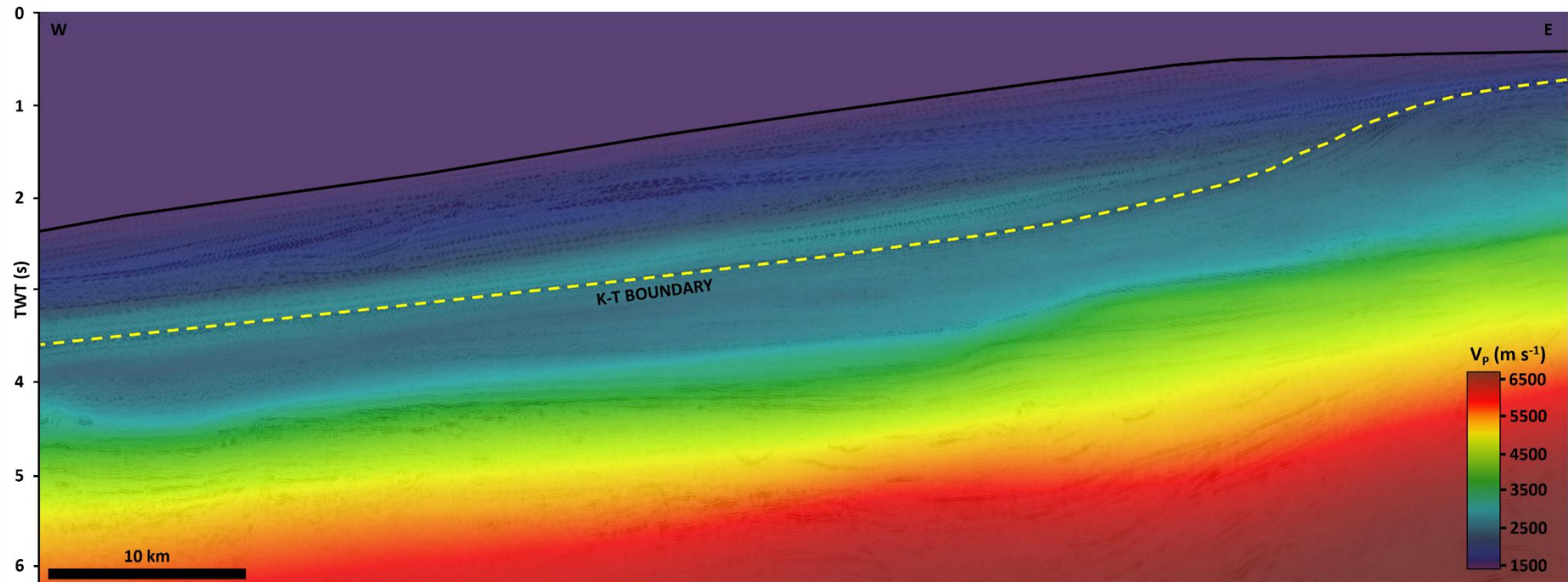


804
 805 *Figure 1: Location map displaying Lüderitz Basin area of interest with available seismic data,*
 806 *using a UTM projection. Key geological, structural and bathymetric features offshore*
 807 *Namibia are highlighted (contour intervals of 500 m [\sim 1640 ft]), adapted from (Bray et al.,*
 808 *1998; Gladchenko et al., 1998; Becker et al., 2009). (a) Inset map displaying extent of seismic*
 809 *data available, mapped BSRs, modelled pseudo wells and transects along which modelling*
 810 *has been conducted. Example open source global heat flow databases are shown in the form*
 811 *of borehole data (Gosnold and Panda, 2002) and Davies (2013) heat flow grid. Regional*
 812 *exploration wells in neighbouring Walvis & Orange Basins are shown for context.*



813
 814 Figure 2: (a) West-East transect displaying two-way travel time (TWT) seismic reflection structure in the Lüderitz Basin. Features visible include
 815 clinoforms in near shore section, with BSR, free gas zone (FGZ) below it highlighted by bright reflectors (associated with gas) and mass
 816 transport features in Tertiary section; (b) Close up of shallow Cenozoic sediments displaying MTD complexes. Cretaceous – Tertiary (K-T)
 817 boundary marked by intense polygonal faulting; (c) Close up of deeper Mesozoic section highlighting intrusive sills beneath a mounded platform
 818 like structure (believed to be a Barremian carbonate reef) overlain by Aptian age "Kudu shale" source rock interval; (d) Close up of SDRs at
 819 depth in the distal section 2D seismic line (Fig. 1a). TWT = Two-way travel time; BSR = Bottom simulating reflector; FGZ = Free gas zone; MTD =
 820 Mass transport deposit; K-T = Cretaceous-Tertiary; SDR = Seaward dipping reflectors.

821



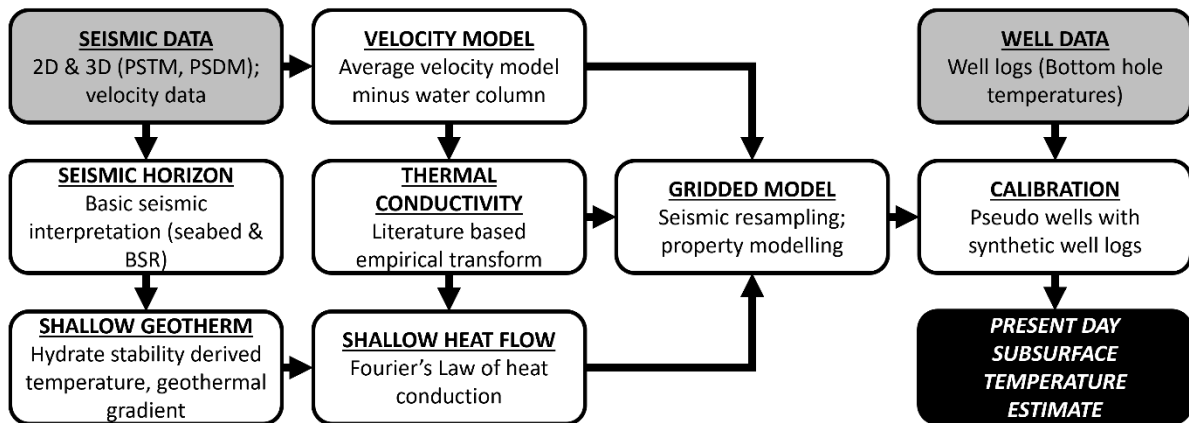
822

823 *Figure 3: West-East transect (Fig. 1) of seismic reflection volume in time domain overlain with interval velocities and K-T boundary highlighted.*

824 *Velocities near seabed (indicated by the black line) are low (close to water velocity). Overall Tertiary section is characterised by low velocities.*

825 *Velocity inversion seen near K-T boundary (yellow dashed line). K-T = Cretaceous-Tertiary.*

826



827

828

829

830

831

832

Figure 4: Schematic summary of the steps involved as part of the seismic led temperature estimation methodology explored in this paper. It utilises an adaptation of the reflection seismic thermometry workflow first presented in (Sarkar, 2020). PSTM = Post Stack Time Migrated; PSDM = Post Stack Depth Migrated; BSR = Bottom Simulating Reflector.



833

834

835

836

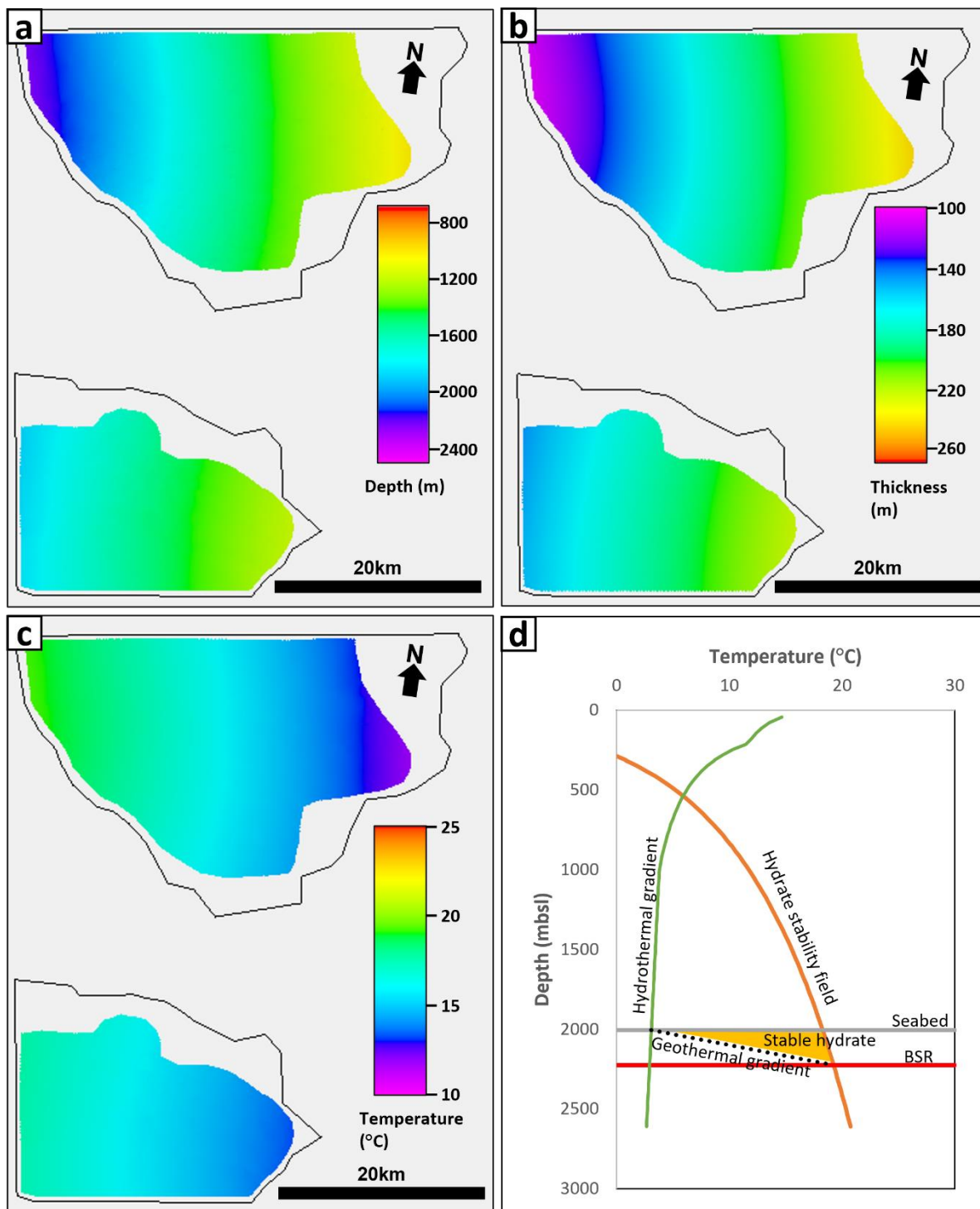
837

838

839

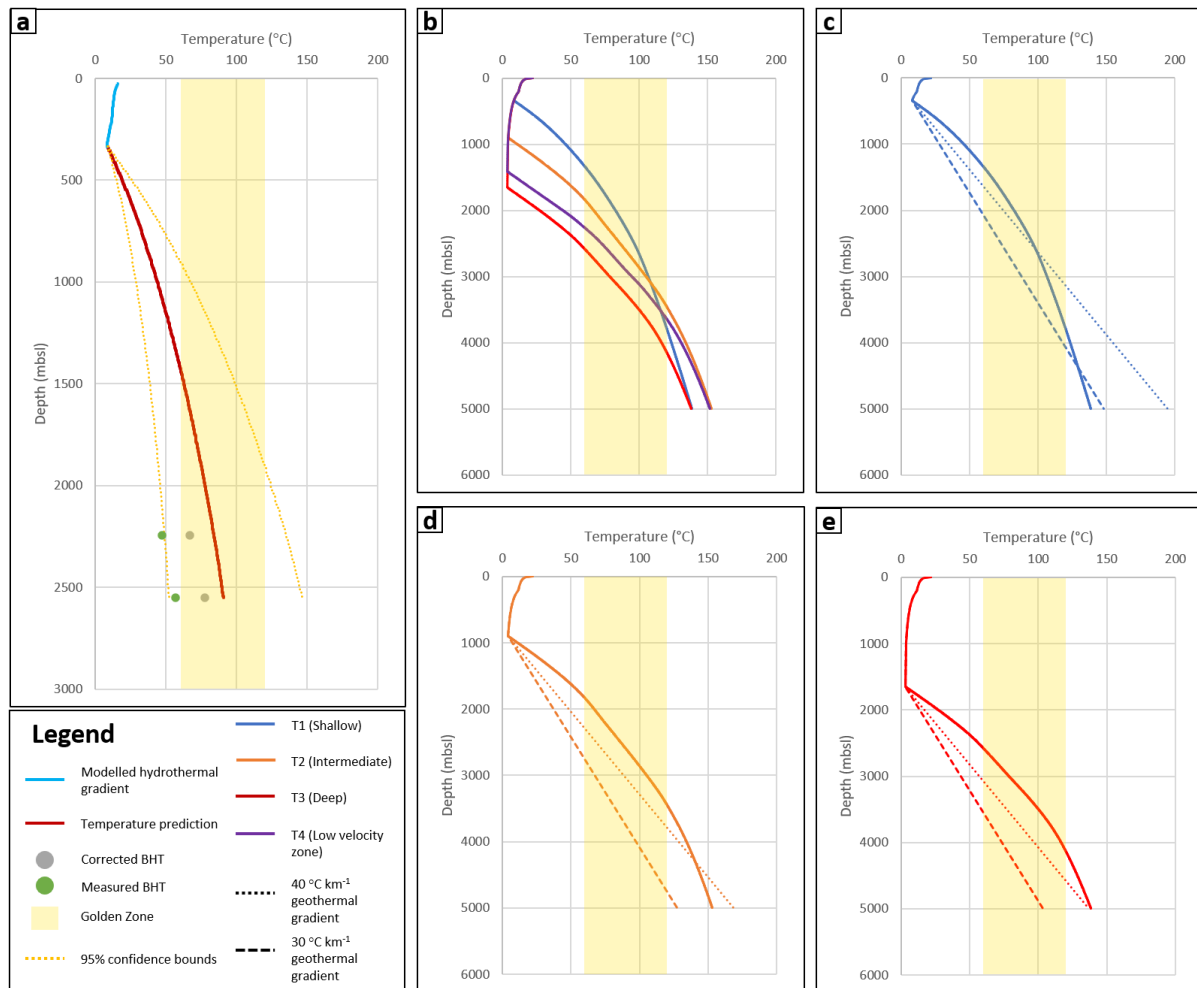
840

Figure 5: Empirical velocity to thermal conductivity transform utilising experimental datasets from published literature. These measurements are made on samples in laboratory conditions and represent a wide range of lithologies. Furthermore, only results from wet sample measurements are displayed, as the transform will be applied in the shallow subsurface where there is very likely to be fluid fill (for example the GHSZ). Measurements were made using transient method (using optical scanning equipment). GHSZ = Gas hydrate stability zone.

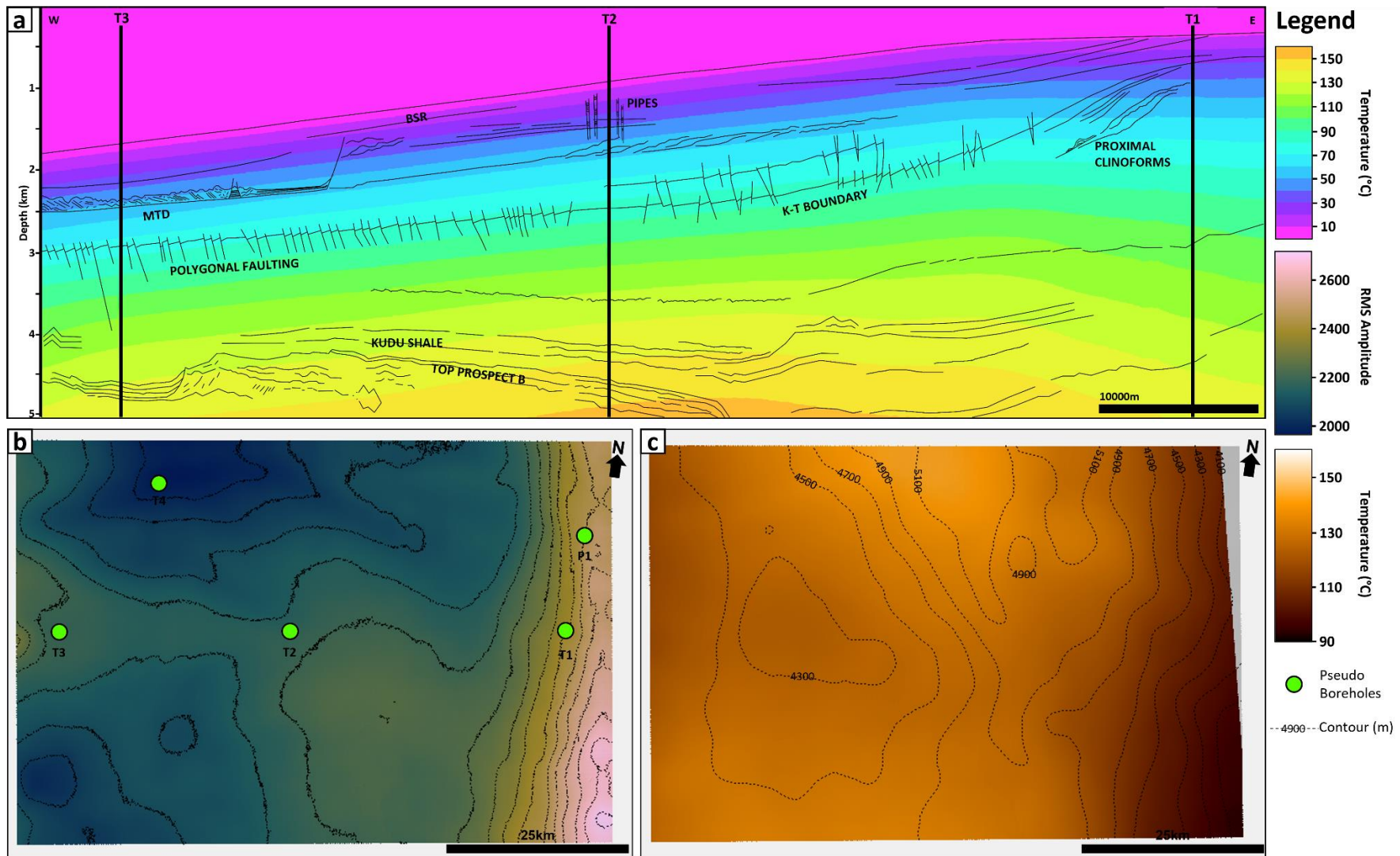


842
 843 *Figure 6: BSR attributes (a – depth; b – GHSZ thickness; & c – temperature at base of GHSZ)*
 844 *are displayed for high confidence area only, with black polygon representing whole BSR*
 845 *interpretation on seismic. (d) Hydrate stability diagram for a pure methane-seawater*
 846 *system, used to compute temperature at the phase boundary (Fig. 6c). A synthetic*
 847 *hydrothermal gradient is shown, computed using the annualised mean temperature data*
 848 *points from the 1 degree resolution dataset of the WOA (Locarnini et al., 2013). The hydrate*

849 stability zone has an average thickness of 184 m (~604 ft) as observed within the study area
 850 (Fig. 6b). The cumulative area of both the mapped BSRs is $0.941 \times 10^9 \text{ m}^2$ ($\sim 1.01 \times 10^{10} \text{ ft}^2$).
 851 Assuming all the sediment above the BSRs contain gas hydrate, a typical hydrate saturation
 852 of 10 % (Waite et al., 2009) would yield a potential methane hydrate volume of $1.73 \times 10^{10} \text{ m}^3$
 853 ($\sim 6.11 \times 10^{11} \text{ ft}^3$). BSR = Bottom Simulating Reflector; GHSZ = Gas Hydrate Stability Zone;
 854 WOA = World Ocean Atlas.
 855



856
 857 **Figure 7: Modelled borehole results for subsurface temperature with Golden Zone interval**
 858 **overlain for reference. (a) Thermal profile for pseudo borehole P1 simulating 2513/8-1 with**
 859 **corrected and uncorrected BHT readings. 95% confidence upper and lower bounds are also**
 860 **displayed. (b) Thermal profile for boreholes T1-T4. (c) T1 shallow water thermal profile with**
 861 **modelled linear geothermal gradients. (d) T2 intermediate water depth thermal profile with**
 862 **modelled linear geothermal gradients. (e) T3 deep water thermal profile with modelled**
 863 **linear geothermal gradients highlights the variability in depth expected for the Golden Zone. BHT =**
 864 **Bottom hole temperature.**
 865



867 *Figure 8: (a) Depth profile with temperature predicted from seismic model overlain. Boreholes corresponding to shallow, intermediate, and*
868 *deep water are marked. (b) RMS velocity extraction of interval velocities (for interval up to 2 s below seabed) highlighting the zone of low*
869 *velocities encountered below the Northern BSR. Borehole T4 specifically targets this. (c) Temperature prediction from the model mapped across*
870 *the base of the Aptian source rock above the mounded structure referred to as Prospect B (Fig. 2c). The thermal model produced was used to*
871 *interrogate the predicted present-day temperature for the base of the source rock interval as shown in Fig. 2c. The temperature ranged*
872 *between 93.2 – 157.2 °C [200 – 315 °F] for a depth range of 3400 – 5400 mbsl [~11155 – 17717 ftbsl]. Scientific colour bar templates based on*
873 *(Cramer et al., 2020). RMS = Root Mean Squared; BSR = Bottom Simulating Reflector; mbsl = metres below sea level; ftbsl = feet below sea*
874 *level.*